ADVANCED FUNCTIONAL MATERIALS
www.afm-journal.de

Bioinspired Wearable Pulse Sensors for Ambulant Cardiovascular Monitoring and Biometric Authentication

Keyu Meng, Zixiao Liu, Xiao Xiao, Farid Manshaii, Pei Li, Junyi Yin, Haiyan Wang, Haixia Mei, Yubo Sun, Ximin He, Jun Yang, and Jun Chen**

The measurement accuracy of current wearable pulse sensors is grandly challenged by motion artifacts caused by body biomechanical activities. In this study, a honeycomb-structure-inspired wearable pulse sensor is reported which not only performs ambulant cardiovascular monitoring but also realizes biometric authentication utilizing the acquired individual pulse wave profiles. The sensor showcases an impressive sensitivity of 46.2 mV Pa^{-1}, a swift response time of 21 ms, and exceptional durability (minimal degradation after 6000 cycles). For practical application in clinical settings, the sensor is able to record pulse signals continuously and accurately from individuals aged between 27 and 57 years, especially including a 29-year-old pregnant woman. Leveraging deep learning algorithms, the sensor further utilizes individual pulse wave profiles for biometric authentication, reaching a classification accuracy of up to 99.4%. The honeycomb-structure-inspired wearable pulse sensor marks a significant advancement in the field of practical cardiovascular monitoring and biometric authentication.

1. Introduction

Cardiovascular diseases (CVDs) continue to be the principal cause of mortality worldwide.[1–4] Arterial pulse waves, offering critical cardiovascular insights like pulse wave velocity, blood pressure, peripheral resistance, and vascular elasticity, are among the most accessible signals for CVD diagnosis.[5–7] The real-time and continuous measurement of pulse waves is crucial for the early prevention of conditions such as hypertension, myocardial infarction, and arteriosclerosis.[8–12] Over recent decades, the development of wearable sensors for continuous pulse monitoring has advanced, incorporating diverse pressure-sensing mechanisms, including piezoelectric,[13–17] piezoresistive,[18–23] capacitive,[24–27] magnetoelastic,[28–31] and triboelectric effects.[32–38] Yet, the broad application of these sensors in cardiovascular monitoring is hindered by motion artifacts caused by human biomechanical movements. These artifacts can compromise signal accuracy and stability, resulting in distorted or unreliable cardiovascular data. To counteract motion artifacts and enhance pulse wave signals, complex signal processing and machine learning algorithms have been adopted.[39,40] However, these advanced methods significantly elevate the system's complexity, energy consumption, and manufacturing cost.

In response, we introduced a honeycomb-structure-inspired (HI) wearable pulse sensor, offering a straightforward, effective, and cost-efficient solution for managing motion artifacts during cardiovascular monitoring. Honeycomb structures, widely recognized for their efficient spatial design and structural stability in nature, serve as the inspiration for this innovation. Bees, for example, employ honeycomb structures in their hives to maximize space efficiency for storing honey and pollen.[41] Similarly, turtle shells feature a honeycomb pattern of small, interlocking bony plates to enhance structural stability.[42,43] By incorporating honeycomb structures into the surface design of pulse sensors, we can improve the signal-to-noise ratio,[44–46] effectively reducing motion artifact interference. Through the application of linear deformation theory and mechanical-electrical finite element simulation, the sensor's deformability, charge induction capacity, and motion artifact resistance have been carefully optimized. The HI wearable pulse sensor exhibits ultrahigh sensitivity (46.2 mV Pa^{-1}), rapid response (≈21 ms), and exceptional mechanical durability (minimal degradation after 6000 cycles). A miniaturized mobile health monitoring system (MHMS) based on the HI pulse sensor has been developed, demonstrating outstanding performance in real-time pulse wave signal extraction

K. Meng, H. Wang, H. Mei, Y. Sun
School of Electronic and Information Engineering
Jilin Provincial Key Laboratory of Human Health Status Identification and Function Enhancement
Changchun University
Changchun 130022, China
Z. Liu, X. He
Department of Materials Science and Engineering
University of California, Los Angeles
Los Angeles, CA 90095, USA
X. Xiao, F. Manshaii, J. Yin, J. Chen
Department of Bioengineering
University of California, Los Angeles
Los Angeles, CA 90095, USA
E-mail: jun.chen@ucla.edu
P. Li, J. Yang
Chongqing Institute of Green and Intelligent Technology
Chinese Academy of Sciences
Chongqing 400714, China
E-mail: jyang@cigit.ac.cn

The ORCID identification number(s) for the author(s) of this article can be found under https://doi.org/10.1002/adfm.202403163

DOI: 10.1002/adfm.202403163

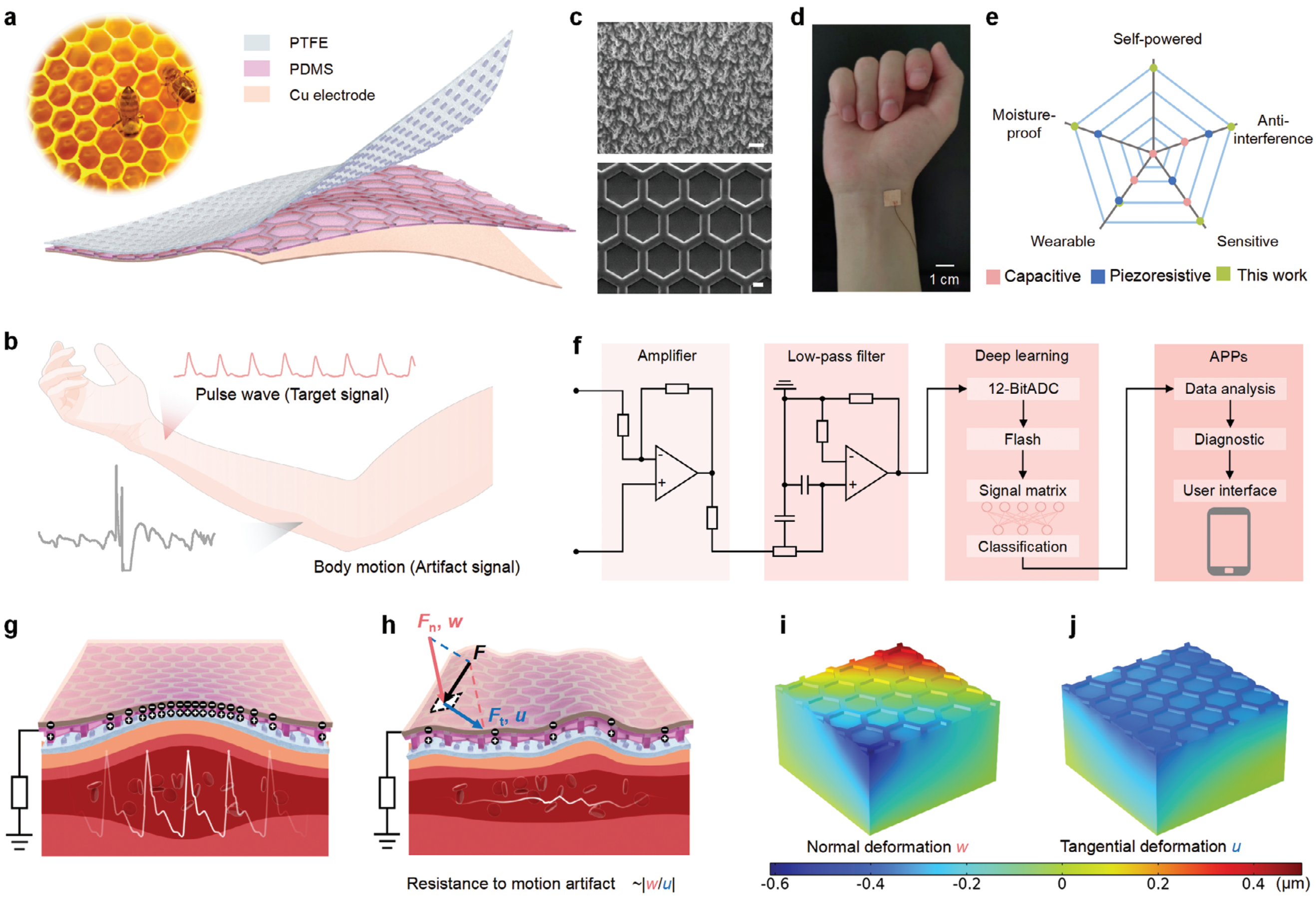

Figure 1. Honeycomb-structure inspired wearable pulse sensors for ambulant pulse wave measurement. a) Schematic of the honeycomb-inspired wearable pulse sensor. b) How structure optimization maximizes subepidermal pulse wave signals while minimizing motion artifact noise. c) SEM images of the PTFE nanowires and the PDMS layer's honeycomb structure. d) Photograph of the fabricated HI wearable pulse sensor worn on the wrist (Scale bar: 1 cm). e) Comparison of the characteristics between conventional pulse sensors and the HI wearable pulse sensor. f) Schematic diagram of the HI wearable pulse sensor based MHMS, highlighting its four main components: data acquisition, signal processing, wireless transmission, and signal display. g,h) Optimized resistance against motion artifacts by increasing deformability in the normal direction w and enhancing the signal-to-noise ratio $|w/u|$. i,j) Normal and tangential deformation of the sensor when subjected to a load in an arbitrary direction.

from various body parts of participants under different physical activity levels. These signals have been successfully utilized for effective cardiovascular monitoring and biometric authentication, achieving a classification accuracy of up to 99.4%. With its innovative design and robust sensing capabilities, the HI wearable pulse sensor is poised to become a revolutionary tool in smart, personalized healthcare technology.

2. Results and Discussion

2.1. Structure Design

The design of the HI wearable pulse sensor is depicted in **Figure 1a**, aiming to optimize pulse wave signal capture while minimizing the impact of motion artifacts (Figure 1b). This ensures precise pulse wave detection even under vigorous movement, achieving optimal signal-to-noise ratio. Polytetrafluoroethylene (PTFE) and polydimethylsiloxane (PDMS) were chosen for the triboelectric layers due to their exceptional triboelectric properties, flexibility, and manufacturability. To boost deformability, surface area, and motion artifact resistance, various PDMS surface constructions were fabricated through mold casting. The mold, featuring microstructures, was prepared on a poly(ethylene terephthalate) (PET) substrate through photolithography, using AZ1500 photoresist from AZ Technology, USA. PDMS precursor was then cast into this mold to produce diverse surface textures. The fabrication process is detailed in Figure S1 (Supporting Information). Furthermore, to enhance the sensor's output performance and sensitivity, a nanowire array was introduced on the PTFE surface via plasma etching. Scanning electron microscopy (SEM) images show the PTFE nanowires and PDMS surfaces with three different constructions in Figure 1c and Figure S2 (Supporting Information). The PTFE and PDMS layers were bonded at the device's four corners using optical clear adhesive (OCA), creating air gaps between the patterns. A 100 nm thick copper (Cu) layer was sputtered onto the backside of the triboelectric layers to act as the electrode. Figure 1d shows the as-fabricated flexible HI wearable pulse sensor worn on the wrist, with dimensions of $1 \times 1 \times 0.014$ cm^3 (Figure S3, Supporting Information), highlighting its excellent conformality and flexibility. Compared to existing pulse sensors, the HI wearable pulse sensor offers significant advantages in sensitivity, anti-interference capabilities, wearability, self-powering, and moisture resistance (Figure 1e).

To enhance the sensor's practical application, an MHMS was developed for the continuous measurement of pulse waves, as illustrated in Figure 1f and Figure S4 (Supporting Information). The MHMS integrates the HI wearable pulse sensor for capturing epidermal pulse signals, an analog signal processing circuit, an analog-to-digital conversion (ADC) unit, and a Bluetooth module for wireless signal transmission to a custom app. This system not only streamlines user interaction but also facilitates real-time health monitoring and data analysis, underscoring the sensor's potential in advancing personal healthcare technologies.

2.2. Working Principle

Based on the triboelectrificaiton between two dissimilar materials, the performance of HI wearable pulse sensors is significantly influenced by the surface morphology, which involves a synergy of structural deformability, surface charge induction, and resistance to motion artifacts. This work introduces a comprehensive theory that merges thin-plate deformation theory, 2D packing efficiency, motion artifact analysis, and electromechanical finite element simulations, offering a holistic view beyond the typical frameworks that focus on isolated aspects.

The principle aims to enhance pulse wave signal capture by maximizing the contact between triboelectric layers, thereby enlarging the effective area for charge induction. This necessitates greater deformability in the direction perpendicular to the device's surface, facilitating the contact-separation process. Our structure optimization model evaluates the deformation characteristics of various polygonal structures—triangles, squares, and honeycombs—under identical circumferences C or areas A, taking into account the small-deflection bending of thin plates under distributed load f. Utilizing Marcus membrane analog,[47] the inherent geometric symmetry of regular polygons, and a point-matching method, we derived a concise formula for maximum deformation expressed as:

$$w_{\max} = 12kf R^4 \left(1 - \nu^2\right) / \mathrm{Eh}^3 \tag{1}$$

Here, k is a geometry-related parameter, and R is the radius of a circumscribing circle around the polygons (Figure S5, Supporting Information). Given consistent material properties and external pressure across structures—such as Young's modulus E, Poisson's ratio ν, thickness h, and load f—the optimization parameter becomes kR.^{4} The comparisons of k, R, and maximum deformation $w_{\max}$ for equilateral triangular, square, and honeycomb configurations, all sharing identical circumferences C or areas A, can be referred to Table S1 (Supporting Information). The honeycomb structure outperforms triangles and squares in deformability, showing up to 1.49 times more deformation than squares and 3.33 times more than triangles for the same circumference, and 1.12- and 1.49-time greater deformability than squares and triangles, respectively, for identical areas. The detailed derivation and solving procedure are elaborated in the Supplementary Information.

Structure optimization extends beyond the microscale of individual units to the macroscale, where numerous units are arranged within a finite space. Hexagonal, or closest-packed, configuration is recognized in mathematics as a highly space-efficient arrangement. However, the efficiency of space utilization varies among different structures (e.g., triangles, squares, honeycombs, and circles) even when employing this hexagonal packaging strategy. Previous literature indicates that honeycomb structures achieve the highest packing density in a hexagonal arrangement by aligning seamlessly side by side without leaving any gaps.[48] Conversely, as the number of edges in polygonal structures increases from six towards infinity (approaching circular shapes), their packing density decreases to below 91%. This reduction is due to the formation of concave-triangular voids between the circles (Figure S6, Supporting Information). Thus, honeycomb structures are optimal not just on the microscale level of individual units but also on the macroscale level of multiple units, showcasing exceptional space utilization efficiency reminiscent of natural beehives.

In addressing motion artifacts, particularly during intense physical activities, the triboelectric layers need to avert unwanted deformation that could engender noise and motion artifacts. Utilizing numerical simulations via the COMSOL solid mechanics module, external pressure was applied to the HI wearable pulse sensor from various directions, as shown in Figure 1g,h. This external load F can be dissected into force components along the normal n and tangential t directions of the device. The component F_n aids in effective signal generation (Figure 1g), whereas F_t causes misalignment of the triboelectric layers, thus generating motion artifacts (Figure 1h). The resistance to motion artifacts is quantified by the ratio of deflection along the normal and tangential directions, symbolized as $|w/u|$. In scenarios where F_t matches F_n in magnitude—an unlikely occurrence in practical applications—the resistance to motion artifacts $|w/u|$ for the honeycomb configuration stands at 1.55 (Figure 1i,j), marking a 6–8% enhancement in performance compared to the square configuration (Figure S7, Supporting Information).

To better understand the mechanical-electrical coupling in the HI wearable pulse sensor, simulations were conducted using COMSOL to determine the theoretical output signals. The sensor was modeled as a capacitor, where PTFE generates positive charges and PDMS produces negative charges. The air gap between these materials acts as a dielectric layer. Upon applying pressure to the sensor, the distance between the PTFE and PDMS layers changes due to deformation (analyzed using the Solid Mechanics module), affecting the capacitance and resulting in an electrical potential difference (Figure S8, Supporting Information) (analyzed with the Electrostatics interface). This potential difference, in an open-circuit setup, is estimated using the formula $\Delta V_\mathrm{oc} = \sigma w/\epsilon_0$, and the mechanical–electrical coupling is further modeled using the Moving Mesh module.

When a pressure of 1 kPa is applied to the sensor, its honeycomb structure exhibits the most significant deformation compared to the other two geometrical designs (Figure S9, Supporting Information). The variations in open-circuit voltage (V_{oc}) across the triboelectric layers, corresponding to different designs, are shown in **Figure** 2a–c. Notably, the V_{oc} of the sensor with a honeycomb design was 1.31 times higher than that of the sensor with a rectangular design. This enhanced sensitivity is attributed

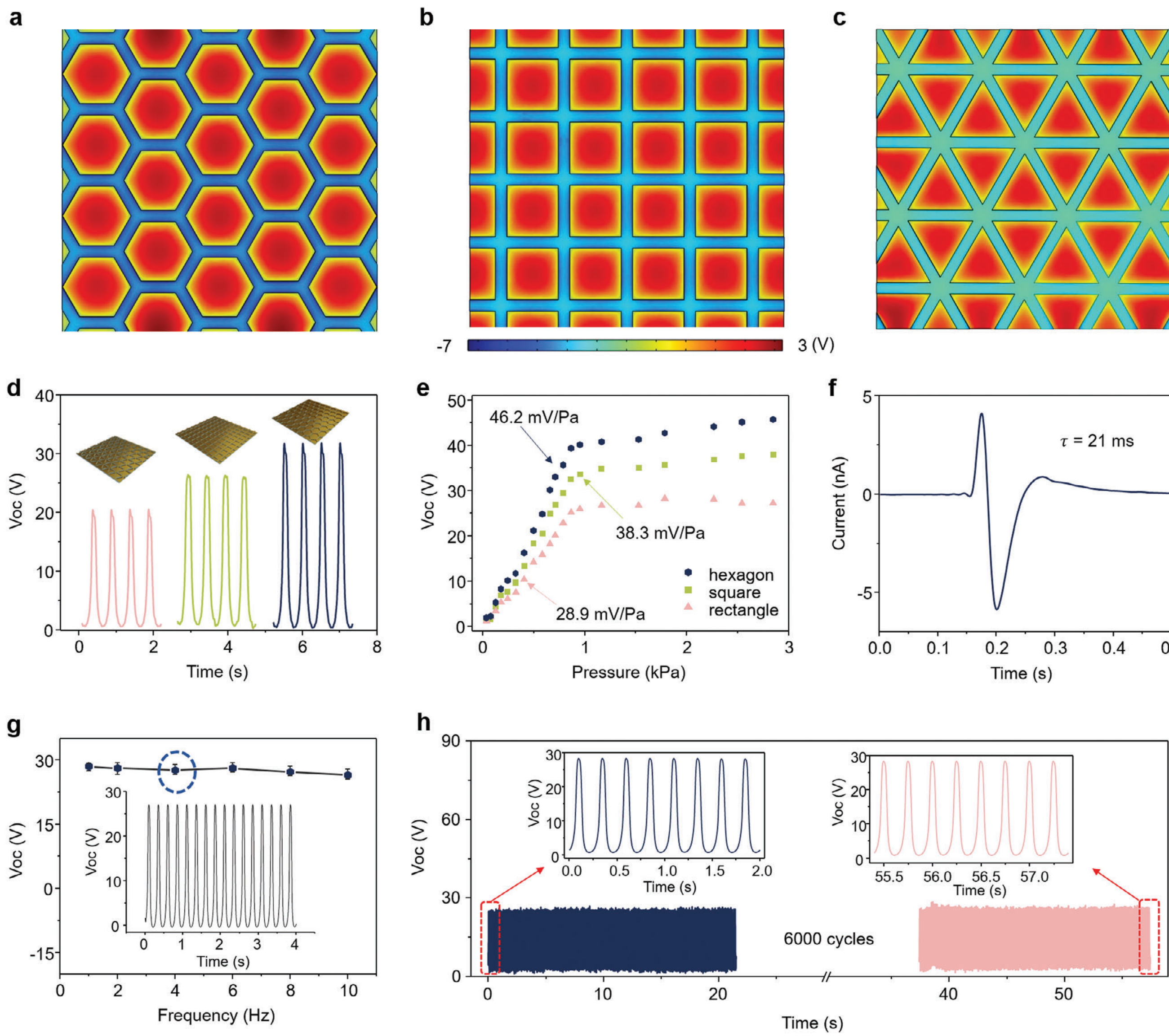

Figure 2. Sensing performance evaluation. electromechanical simulation results showing the distribution of V_{oc} under a 1 kPa normal pressure for three structural designs: a) honeycomb, b) square, and c) equilateral triangle. d) experimental measurements of V_{oc} across different structural designs. e) V_{oc} of the HI wearable pulse sensor across a range of pressures, from 3 Pa to 3 kPa. f) Time response of the HI wearable pulse sensor. g) V_{oc} variation of the HI wearable pulse sensor at different contact frequencies, ranging from 1 to 10 Hz. h) Real-time V_{oc} of the HI wearable pulse sensor over 6000 loading/unloading cycles, showing no observable performance degradation.

to its superior deformability and a larger effective contact area for generating triboelectric charges. The integration of finite element simulation with structural optimization theory provides a comprehensive method and a logical design principle for predicting the performance of the HI wearable pulse sensor.

2.3. Electrical Output Performance

To quantitatively assess the output performance of the HI wearable pulse sensor, a specialized testing setup featuring a high-precision force gauge and a vibration shaker was developed, as shown in Figure S10 (Supporting Information). The sensor's output was systematically evaluated across three structural designs under constant pressure of 700 Pa, detailed in Figure 2d. Compared to the honeycomb-inspired configuration, both the triangular and square designs exhibited declined output signals. This decrease was linked to their lesser mechanical deformation and reduced contact area for triboelectric charge generation. The V_{oc} achieved by the sensor reached up to 32.3 V, which is 1.6 times higher than that of the triangular design and 1.2 times that of the square design. The discrepancy in V_{oc} compared to theoretical predictions from Section 2.2 was under 10%.

To verify the sensor's enhanced sensitivity across a broad pressure spectrum, output voltage measurements were taken under varying pressures from 3 Pa to 3 kPa. The honeycomb structure consistently produced higher electrical signals, showing greater sensitivity throughout the test range, as depicted in Figure 2e. The V_{oc} curves revealed two distinct linear behaviors: a rapid response at low pressures and a slower response at higher pressures. The sensor's superior sensitivity was evident, with a measurement of 46.2 mV Pa^{-1} in the 3–800 Pa range. Beyond 800 Pa, the sensitivity decreased to 3.1 mV Pa^{-1}, attributed to the saturation of the effective contact-separation area. Moreover, the sensor's responsiveness was gauged from short-circuit current (I_{sc}) curves at 1 Hz frequency and 600 Pa pressure, showing a fast response time (τ) of 21 ms in Figure 2f. Given the sensor's design for skin compatibility, it needs to be flexible and adhere well to human skin. Figure S11 (Supporting Information) demonstrates the sensor's stability through repeated bending tests, showing negligible output voltage change across bending radii of 1–5 mm.

Frequency response tests, illustrated in Figure 2g, affirmed that the sensor sustained stable output voltage over a frequency range of 1–10 Hz. Detailed data in Figure 2g indicated its effective operation at 4 Hz, aligning with the requirement to accurately capture pulse wave characteristics, predominantly consisting of low-frequency components. Furthermore, mechanical durability for long-term pulse monitoring was examined through cyclic loading-unloading tests at a constant pressure of 600 Pa, as demonstrated in Figure 2h. In addition, we conducted continuous testing over 5 days, performing over 6000 loading/unloading cycles each day, as shown in Figure S12 (Supporting Information). The sensor exhibited minimal V_{oc} variation even after ≈6000 loading/unloading cycles, underscoring its remarkable durability and consistency. Therefore, the honeycomb structure's stability significantly contributes to the sensor's sustained, high-quality performance over extended periods of practical use.

2.4. Motion Artifact Resistance and Ambulant Biomonitoring

To mitigate motion artifacts, which can cause misinterpretations in wearable electronics, particularly during physical activities, we studied the HI wearable pulse sensor's resistance to two main types of motion: a) large amplitude, long-duration movements (e.g., body movements), representing a sustained, continuous signal input; and b) small amplitude, short-duration movements (e.g., fetal movements), representing an impulsive signal. These motions require the device to possess exceptional structural stability to prevent damage and misalignment of triboelectric layers for type a) motions, and high elasticity with minimal viscoelasticity for quickly adapting to type b) motions.

To evaluate the sensor's performance against type a) motion, tests including wrist rotation and finger bending were conducted while monitoring the epidermal pulse signal, illustrated in **Figure 3**a,b. Despite the significant bending angles of up to 90°, the slow speed of these movements allowed the sensor to accurately capture cardiac cycles, including peak points, without any observable structural damage or misalignment, as shown in Figure 3c,d. This demonstrated the sensor's capability for precise pulse monitoring under large amplitude motion.

The study extended its investigation to measure the pulse signals of two participants—a 29-year-old pregnant woman and a 53-year-old woman—in different postures to further validate the versatility and efficacy of the HI wearable pulse sensor for real-life application. Before data recording, each participant was instructed to maintain sitting and standing postures for 12 s each, followed by a 10 s jogging session on a treadmill at a speed of ≈4 km h^{-1}. After the brief exercise, participants were required to sit down for 12 s to return to a restful state. It was observed that the pulse waveforms captured by the HI wearable pulse sensor showed significant fluctuations during jogging, while the readings remained relatively stable during the sitting, standing, and recovery phases. The beat-to-beat heart rates calculated for each participant were shown in Figure 3e and Figure S13 (Supporting Information), respectively. To verify the universality of the sensor, we selected four participants and measured their pulse signals under different postures, as shown in Figure S14 (Supporting Information). It was observed that the pulse waveforms captured by the HI wearable pulse sensor showed significant fluctuations during jumping, while the readings remained relatively stable during the sitting, walking, and recovery phases, during which the peak of the pulse waveforms can be clearly distinguished. Furthermore, to assess whether the HI wearable pulse sensor is suitable for long-term pulse monitoring, we measured pulse signals in various postures to demonstrate its durability and practical application. Figure S15 (Supporting Information) demonstrates tens of seconds of pulse in each state, which indicates that our sensor can achieve long-term pulse signal monitoring.

Additionally, by extracting a one-period pulse waveform for each posture and comparing them in Figure 3f, a typical characteristic pulse waveform was identified, featuring three distinguishable points: systolic pressure (P1), an inflection point (P2), and diastolic pressure (P3). It was noted that the amplitude of pulse waves and the heart rate increased with the intensity of physical activity. The effect of perspiration on epidermal sensors is non-negligible.[49,50] To further validate the robustness of our sensor during perspiration and intense physical exercise, we mixed a modest quantity of sand into a saline solution and applied this mixture to the wrist surface to simulate the dirt and sweat on the skin (Figure S16a, Supporting Information). The measured pulse signals before and after applying the mixture are shown in Figure S16b,c (Supporting Information), respectively. The radial pulse signals of the same participant can be precisely captured before and after applying the mixture. The critical characteristic points (P1, P2, and P3) of the pulse waveforms can be clearly distinguished. In addition, by extracting a single-period pulse waveform of each group and comparing them in Figure S16d (Supporting Information). Two pulse waveforms have a high similarity with R = 0.9958, which indicates that the proposed HI sensor can be successfully applied in pulse measurement during perspiration and physical exercise.

In exploring the sensor's applicability for individuals requiring special monitoring, such as pregnant women, a 3 min pulse signal measurement was conducted with the 29-year-old pregnant participant wearing the sensor on her wrist, as depicted in **Figure 4**b and demonstrated in Movie S1 (Supporting Information). The pulse waveforms recorded are displayed in Figure 4c. Fetal movement, a critical indicator for monitoring fetal health, was also tracked. Unlike sustained or continuous motions, fetal movements are characterized by small amplitudes and occur instantaneously, making them challenging to accurately capture due to susceptibility to motion artifacts. Fetal movements were recorded over 5 minutes, as shown in Figure 4a,d with the

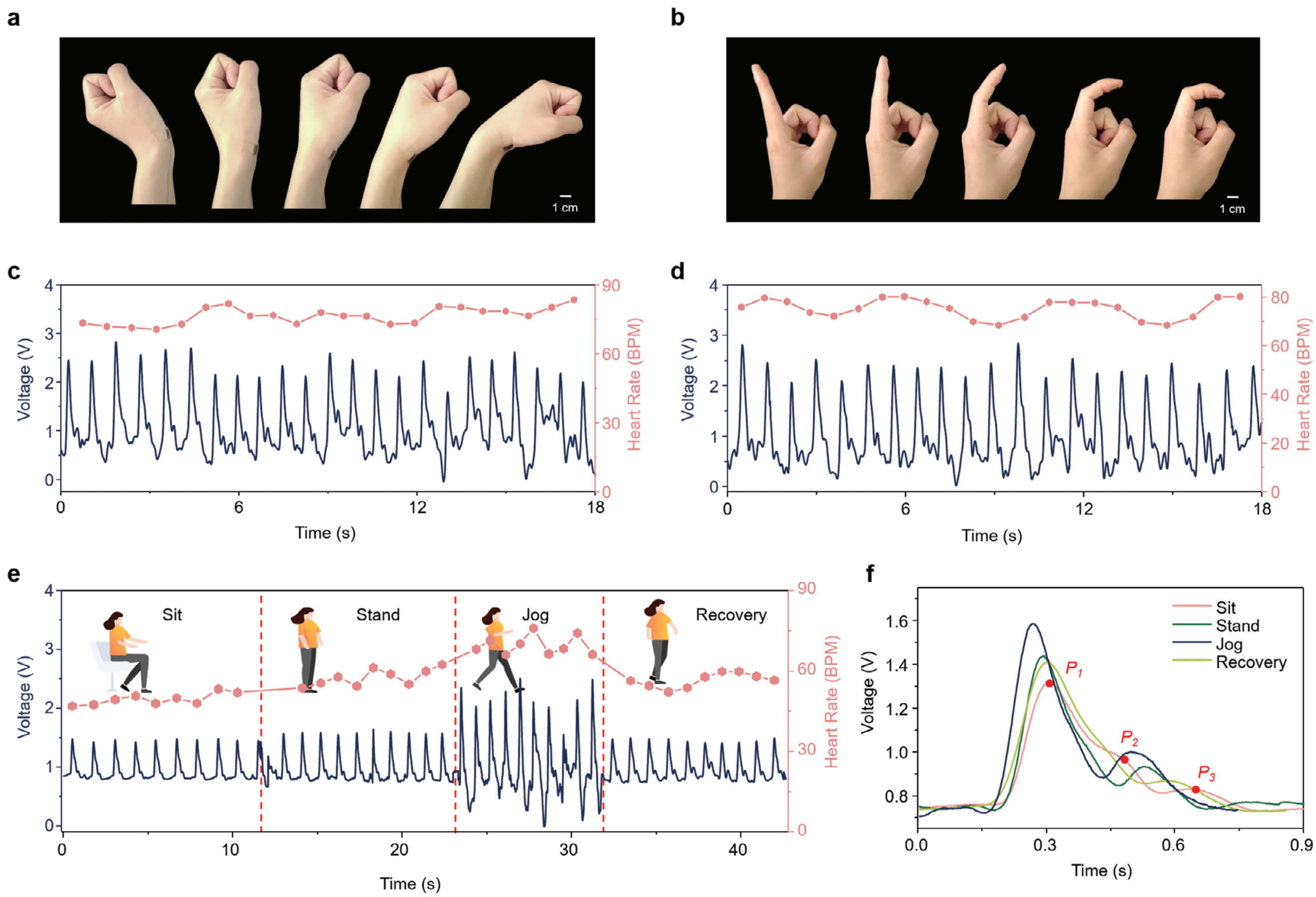

Figure 3. Stable pulse wave monitoring with daily biomechanical motions. a,b) Photographs of the HI wearable pulse sensor worn on the a) wrist and b) fingertip. c,d) Epidermal pulse signal and beat-to-beat heart rate during c) wrist rotation and d) finger bending. e) Continuous monitoring of pulse waveform and heart rate during physical activities. f) One-period pulse waveforms were captured in different postures: sitting, standing, jogging, and recovery.

findings documented in Movie S2 and S3 (Supporting Information). The results highlighted that the sensor maintained stable respiratory waveforms in the absence of fetal movement. However, waveforms were notably disturbed during fetal movements, as marked by the red dotted box in Figure 4e. The data on horizontal and vertical coordinates provided insights into the speed and strength of fetal movements, respectively. Measurements of pulse waveforms of the pregnant at various stages of pregnancy (29–36 weeks) were depicted in Figure S17 (Supporting Information), confirming that the HI wearable pulse sensor's performance remains consistent across different durations and intensities of motion signals. Its exceptional elastic response ensures its effectiveness in a wide range of applications, from pulse monitoring to tracking fetal movements in pregnant individuals, highlighting its reliability and broad utility in health monitoring scenarios.

Continuous pulse wave monitoring was carried out on a 19-week pregnant individual over 14 h of daytime activities, illustrating the practical application and robustness of the HI wearable pulse sensor in real-world settings. The participant's location was tracked using a mobile phone Global Positioning System (GPS) application throughout the day, which identified three major location changes: bicycling from home to the laboratory (T_1), walking from the laboratory to the canteen (T_2), and strolling from the laboratory to the park (T_3), as detailed in Figure 4f. The heart rate variations of the pregnant participant, derived from the pulse waveforms are presented in Figure 4g. These pulse wave signals, showcased in Figure 4h, revealed notable differences in signal fluctuation corresponding to the varying intensities and types of activities undertaken by the participant. Specifically, during bicycling, the pulse signals exhibited more pronounced fluctuations due to the combined effects of motion artifacts and external environmental disturbances. In contrast, when the participant was walking to the canteen or strolling in the park, the pulse signals were considerably more stable, likely due to the more consistent pace of walking. These observations suggest that the fabricated MHMS represents an effective alternative for the health monitoring of pregnant women during their daily routines, offering a less cumbersome option compared to traditional, bulky hospital equipment.

2.5. Biometric Authentication

To achieve biometric authentication using extracted pulse signals, the study integrated data collected from the HI

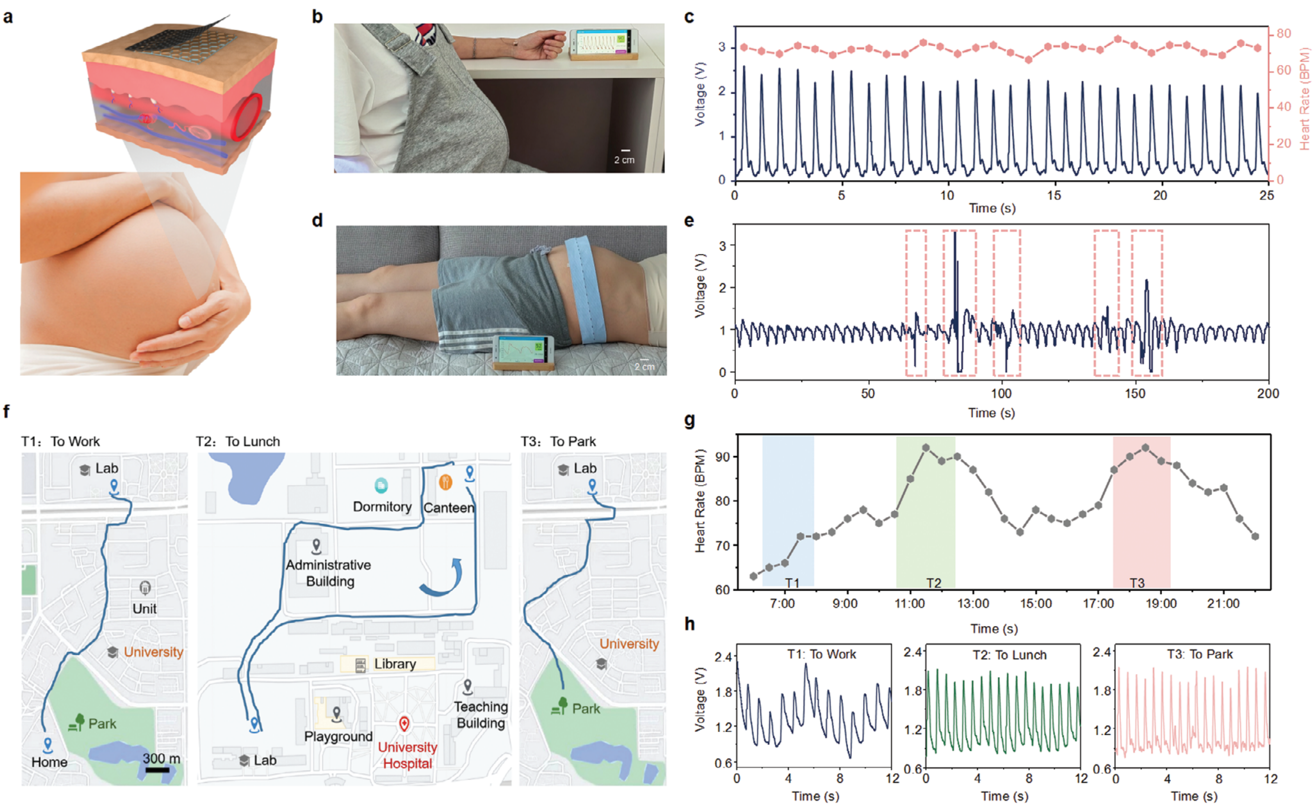

Figure 4. Continuous pulse wave monitoring in a pregnant individual. a) Illustration depicting HI wearable pulse sensor deployment for fetal movement detection. b) Wrist-worn HI wearable pulse sensor for monitoring pulse waves. c) Pulse waveforms and heart rate data captured by the sensor. d) Tracking fetal movements using the HI wearable pulse sensor placed on the abdomen. e) Breathing waveforms showing variations in fetal movement amplitude. f) GPS map tracking the subject's position. g) Heart rate data collected over a day by the MHMS. h) Detailed pulse wave signals acquired by the HI wearable pulse sensor.

wearable pulse sensor with convolutional neural networks (CNNs) (**Figure 5a**). As shown in Figure S18 (Supporting Information), a three-layer 1D-CNN was designed for feature extraction and automatic identification of pulse waveforms, demonstrating the potential of the HI wearable pulse sensor in personal healthcare monitoring systems. The study involved measuring the pulse waveforms of 24 participants across different age groups to showcase the sensor's capability. We conducted pulse monitoring at three different times of the day—morning, noon, and evening—while the participants were either stationary or walking. Notably, the participants were asked to have a completely relaxed state for 5–10 min and keep sitting for 3 min for the stationary test. In addition, subjects were asked to walk at a suitable pace to monitor their pulse signals during walking. The pulse signal measurement was conducted with the participant wearing the sensor on the wrist. Finally, relatively stable sections of the measurement pulse waveforms were selected for training purposes. As shown in Figure 5b–e, four participants aged 27, 34, 46, and 57 years, were selected for extended pulse monitoring to illustrate the sensor's effectiveness in capturing distinct biometric features. The CNN model processed the extracted digital features through multilayer analysis. Data samples were divided into training and testing sets at an 8:2. Figure 5f displays the evolution of training and testing accuracy, along with the loss function, indicating the model's ability to achieve high classification accuracy and robustness. After 200 training epochs, the model reached its maximum classification accuracy. The confusion matrix, presented in Figure 5g after 200 rounds of training, demonstrates the system's high precision in identifying different participants, with an average prediction accuracy of 99.4%.

3. Conclusion

In this study, we introduced a honeycomb-inspired wearable pulse sensor system designed for the continuous monitoring of cardiovascular health and as a precautionary measure against CVDs. This miniaturized mobile monitoring system, notable for its compact size of $1 \times 1 \times 0.014$ cm^3, demonstrated exceptional sensitivity at 46.2 mV Pa^{-1} in low-pressure regions and a broad frequency response capable of precisely capturing characteristic points of pulse waves. Its designs ensure high mechanical robustness and electrical reliability, maintaining performance integrity even after 6000 cycles of continuous mechanical operation. The HI wearable pulse sensor system excels in accurately capturing human pulse waves and heart rates, effectively eliminating interferences from external environmental factors during physical activities. Moreover, this system goes beyond mere pulse wave signal measurement; it offers a continuous, non-invasive method for arteriosclerosis prognosis, significantly enhancing convenience for users. Characterized by its flexibility, durability,

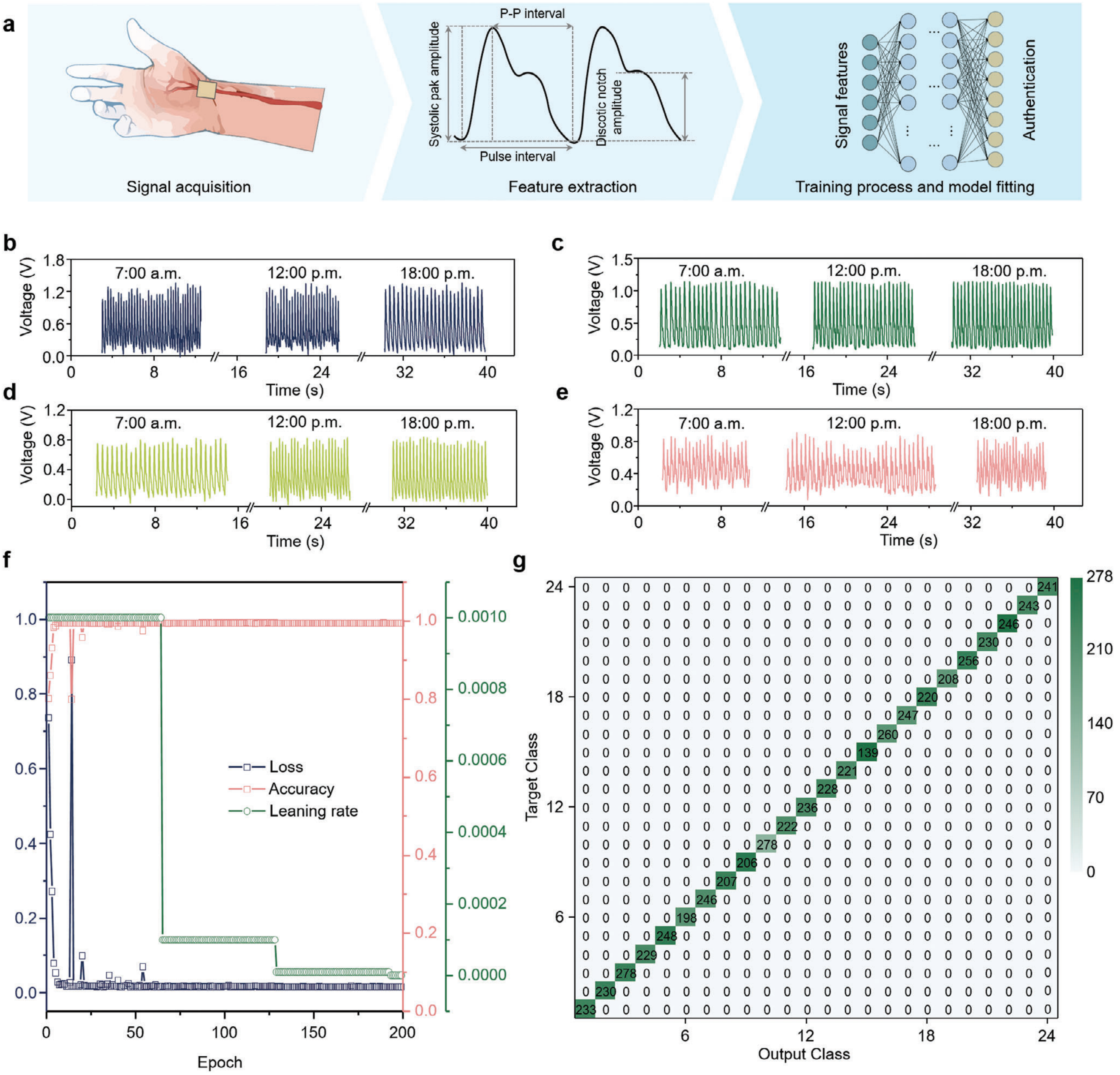

Figure 5. Pulse wave profile for biometric authentication. a) Workflow and structure of the CNN. Continuous pulse waveform monitoring for individuals of varying ages: b) 27 years old, c) 34 years old, d) 46 years old, and e) 57 years old. f) Classification accuracy, learning rate, and loss metrics of the training process. g) Confusion matrix comparing predicted versus true labels in the testing set after 200 training rounds.

and sensitivity, this study heralds a new era of cost-effective, remote monitoring of human movement, pulse waves, and overall health. It stands as a promising alternative to conventional commercial bracelets, particularly benefiting athletes and the elderly. This miniaturized mobile monitoring system not only marks a significant advancement in the design of flexible pressure sensors for real-time monitoring of human physical activities but also contributes to the development of more comfortable, nonintrusive platforms for remote healthcare monitoring. In summary, the honeycomb structure employed in this study could not only improve the sensitivity of pulse sensors but also enhance the signal-to-noise ratio as well as the resistance to motion artifacts.

4. Experimental Section

Fabrication of Nanowire Array on PTFE Surface: A PTFE film, 25 µm in thickness, was cleaned using menthol, isopropyl alcohol, and deionized water. The aligned nanowires were then fabricated on the PTFE surface using a reactive-ion etching (RIE) system. O_2 gas was introduced into the RIE chamber at a flow rate of 30.0 sccm, with 100 W serving as the power source for plasma ion acceleration. The PTFE nanowires (nPTFE) were produced after a reaction time of ≈10–15 min.

Manufacturing Process of the Structure-Optimized Layer: To create a mold with microstructures, a positive photoresist (AZ1500, sourced from AZ Technology, America) was spin-coated onto a smooth PET surface. The spin-coating process involved speeds of 500 rpm for 5 s, 2000 rpm for 25 s, and 3000 rpm for 5 s. After curing at 80 °C for 15 min, the coated PET underwent exposure in a mask aligner (ABM/6/350/NUV/DCCD/BSV/M, America) for 8.5 s and was then developed in a developer solution (AZ351B, purchased from AZ Technology, America) for 30 s to create a microstructure template. A PDMS precursor (SYLGARD 184 purchased from Dow Corning, America), mixed at a 1:10 weight ratio, was cast into the template to transfer the photolithography structure flexibly.

Assembly of the Construction-Optimized Device: The patterned PET and PTFE layers were bonded using optical clear adhesive (OCA) at the device's four corners. An air gap naturally formed between the patterns. A 100 nm thick Cu layer was sputtered onto the backside of the triboelectric layers to serve as electrodes.

Experimental Setup for Pressure and Electrical Characterization: The multilevel micro-constructed PDMS and nanowire-patterned PTFE were characterized using a JEOL JSM-7800F SEM. A well-defined sinusoidal load was applied using a function generator (Stanford DS345) and an amplifier (LabworkPa-13). An electrometer (Keithley 6514) was used to measure and record the V_{oc} and I_{sc} of the MMTPS. External pressure was gauged using a dual-range force gauge (DSM-2).

Human Subject Study: The wearable pulse sensor used for cardiovascular monitoring was tested on human subjects in accordance with all ethical regulations, under a protocol approved by the Institutional Review Board at the University of California, Los Angeles (ID: 20–001882). All participants were affiliated with the University of California, Los Angeles, and provided informed consent before participating in the study.

Supporting Information

Supporting Information is available from the Wiley Online Library or from the author.

Acknowledgements

K.M. acknowledges the National Natural Science Foundation of China (NSFC 52205586). J.C. acknowledges the Henry Samueli School of Engineering & Applied Science and the Department of Bioengineering at the University of California, Los Angeles for the startup support. J.Y. acknowledges the National Natural Science Foundation of China (NSFC 52175281) and the Youth Innovation Promotion Association of the Chinese Academy of Sciences (2021382).

Conflict of Interest

The authors declare no conflict of interest

Data Availability Statement

The data that support the findings of this study are available from the corresponding author upon reasonable request.

Keywords

bioinspired, biometric authentication, cardiovascular monitoring, motion artifacts, wearable pulse sensor

Received: February 21, 2024
Revised: June 6, 2024
Published online: June 16, 2024

[1] R. Kelly, C. Hayward, A. Avolio, M. O'rourke, *Circulation* **1989**, *80*, 1652.
[2] X. Zhao, Y. Zhou, Y. Song, J. Xu, J. Li, T. Tat, G. Chen, S. Li, J. Chen, *Nat. Mater.* **2024**, *23*, 703.
[3] G. Chen, C. Au, J. Chen, *Trends Biotechnol.* **2021**, *39*, 1078.
[4] S. Chen, J. Qi, S. Fan, Z. Qiao, J. C. Yeo, C. T. Lim, *Adv. Healthcare Mater.* **2021**, *10*, 2100116.
[5] G. Chen, X. Xiao, X. Zhao, T. Tat, M. Bick, J. Chen, *Chem. Rev.* **2022**, *122*, 3259.
[6] Y. Fang, X. Zhao, T. Tat, X. Xiao, G. Chen, J. Xu, J. Chen, *Matter* **2021**, *4*, 1102.
[7] K. Meng, X. Xiao, W. Wei, G. Chen, A. Nashalian, S. Shen, X. Xiao, J. Chen, *Adv. Mater.* **2022**, *34*, 2109357.
[8] W. Deng, Y. Zhou, A. Libanori, G. Chen, W. Yang, J. Chen, *Chem. Soc. Rev.* **2022**, *51*, 3380.
[9] C. Wang, X. Li, H. Hu, L. Zhang, Z. Huang, M. Lin, Z. Zhang, Z. Yin, B. Huang, H. Gong, S. Bhaskaran, Y. Gu, M. Makihata, Y. Guo, Y. Lei, Y. Chen, C. Wang, Y. Li, T. Zhang, Z. Chen, A. P. Pisano, L. Zhang, Q. Zhou, S. Xu, *Nat. Biomed. Eng.* **2018**, *2*, 687.
[10] C. Dagdeviren, Y. Su, P. Joe, R. Yona, Y. Liu, Y. S. Kim, Y. Huang, A. R. Damadoran, J. Xia, L. W. Martin, Y. Huang, J. A. Rogers, *Nat. Commun.* **2014**, *5*, 4496.
[11] S. Xu, K. Scott, F. Manshaii, J. Chen, *Matter* **2024**, *7*, 1684.
[12] Y. Su, C. Chen, H. Pan, Y. Yang, G. Chen, X. Zhao, W. Li, Q. Gong, G. Xie, Y. Zhou, S. Zhang, H. Tai, Y. Jiang, J. Chen, *Adv. Funct. Mater.* **2021**, *31*, 2010962.
[13] J. Li, H. Jia, J. Zhou, X. Huang, L. Xu, S. Jia, Z. Gao, K. Yao, D. Li, B. Zhang, Y. Liu, Y. Huang, Y. Hu, G. Y. Zhao, Z. Xu, J. Li, C. K. Yiu, Y. Gao, M. Wu, Y. Jiao, Q. Zhang, X. C. Tai, R. H. Chan, Y. Zhang, X. H. Ma, X. Yu, *Nat. Commun.* **2023**, *14*, 5009.
[14] Y. Su, W. Li, L. Yuan, C. Chen, H. Pan, G. Xie, G. Conta, S. Ferrier, X. Zhao, G. Chen, H. Tai, Y. Jiang, J. Chen, *Nano Energy* **2021**, *89*, 106321.
[15] X. Xiao, J. Yin, G. Chen, S. Shen, A. Nashalian, J. Chen, *Matter* **2022**, *5*, 1342.
[16] B. Lan, X. Xiao, A. Di Carlo, W. Deng, T. Yang, L. Jin, G. Tian, Y. Ao, W. Yang, J. Chen, *Adv. Funct. Mater.* **2022**, *32*, 2207393.
[17] Y. Su, W. Li, X. Cheng, Y. Zhou, S. Yang, X. Zhang, C. Chen, T. Yang, H. Pan, G. Xie, G. Chen, X. Zhao, X. Xiao, B. Li, H. Tai, Y. Jiang, L.-Q. Chen, F. Li, J. Chen, *Nat. Commun.* **2022**, *13*, 4867.
[18] Z. Gao, X. Xiao, A. D. Carlo, J. Yin, Y. Wang, L. Huang, J. Tang, J. Chen, *Adv. Funct. Mater.* **2023**, *33*, 2214265.
[19] Y. Li, J. Yin, S. Liu, B. Xue, C. Shokoohi, G. Ge, M. Hu, T. Li, X. Tao, Z. Rao, F. Meng, H. Shi, X. Ji, P. Servati, X. Xiao, J. Chen, *Adv. Sci.* **2023**, *10*, 2206982.
[20] M. R. Islam, S. Afroj, J. Yin, K. S. Novoselov, J. Chen, N. Karim, *Adv. Sci.* **2023**, *11*, 2304140.
[21] Q. Wei, G. Chen, H. Pan, Z. Ye, C. Au, C. Chen, X. Zhao, Y. Zhou, X. Xiao, H. Tai, Y. Jiang, G. Xie, Y. Su, J. Chen, *Small Methods* **2021**, *5*, 2101051.
[22] Y. Si, X. Wang, C. Yan, L. Yang, J. Yu, B. Ding, *Adv. Mater.* **2016**, *28*, 9512.
[23] H. Pan, G. Chen, Y. Chen, A. Di Carlo, M. Mayer, S. Shen, C. Chen, W. Li, S. Subramaniam, H. Huang, H. Tai, Y. Jiang, G. Xie, Y. Su, J. Chen, *Biosens. Bioelectron.* **2023**, *222*, 114999.
[24] X. Zeng, Y. Hu, *ACS Nano* **2021**, *15*, 9238.
[25] C. Pang, J. H. Koo, A. Nguyen, J. M. Caves, M. G. Kim, A. Chortos, K. Kim, P. J. Wang, J. B. H. Tok, Z. Bao, *Adv. Mater.* **2015**, *27*, 634.
[26] A. Libanori, G. Chen, X. Zhao, Y. Zhou, J. Chen, *Nat. Electron.* **2022**, *5*, 142.
[27] Q. Lin, J. Huang, J. Yang, Y. Huang, Y. Zhang, Y. Wang, J. Zhang, Y. Wang, L. Yuan, M. Cai, X. Hou, W. Zhang, Y. Zhou, S. G. Chen, C. F. Guo, *Adv. Healthcare Mater.* **2020**, *9*, 2001023.

[28] Y. Zhou, X. Zhao, J. Xu, Y. Fang, G. Chen, Y. Song, S. Li, J. Chen, *Nat. Mater.* **2021**, *20*, 1670.
[29] G. Chen, X. Zhao, S. Andalib, J. Xu, Y. Zhou, T. Tat, K. Lin, J. Chen, *Matter* **2021**, *4*, 3725.
[30] J. Xu, T. Tat, J. Yin, D. Ngo, X. Zhao, X. Wan, Z. Che, K. Chen, L. Harris, J. Chen, *Matter* **2023**, *6*, 2235.
[31] X. Zhao, Y. Zhou, J. Xu, G. Chen, Y. Fang, T. Tat, X. Xiao, Y. Song, S. Li, J. Chen, *Nat. Commun.* **2021**, *12*, 6755.
[32] S. Zhang, M. Bick, X. Xiao, G. Chen, A. Nashalian, J. Chen, *Matter* **2021**, *4*, 845.
[33] S. Shen, X. Xiao, J. Yin, X. Xiao, J. Chen, *Small Methods* **2022**, *6*, 2200830.
[34] J. Yin, S. Wang, A. Di Carlo, A. Chang, X. Wan, J. Xu, X. Xiao, J. Chen, *Med-X* **2023**, *1*, 3.
[35] Y. Fang, Y. Zhou, J. Xu, G. Cheng, Y. Zhou, W. Deng, X. Zhao, M. Roustaei, T. K. Hsiai, J. Chen, *Adv. Mater.* **2021**, *33*, 2104178.
[36] J. Xu, J. Yin, Y. Fang, X. Xiao, Y. Zou, S. Wang, J. Chen, *Nano Energy* **2023**, *113*, 108524.
[37] J. Yin, V. Kashyap, S. Wang, X. Xiao, T. Tat, J. Chen, *Device* **2024**, *2*, 100252.
[38] K. Meng, S. Zhao, Y. Zhou, Y. Wu, S. Zhang, Q. He, X. Wang, Z. Zhou, W. Fan, X. Tan, J. Yang, J. Chen, *Matter* **2020**, *2*, 896.
[39] J. Yin, S. Wang, T. Tat, J. Chen, *Nat. Rev. Bioeng.* **2024**, https://doi.org/10.1038/s44222-024-00175-4.
[40] X. Xiao, Y. Fang, X. Xiao, J. Xu, J. Chen, *ACS Nano* **2021**, *15*, 18633.
[41] H. Wang, J. Wang, D. Cao, H. Gu, B. Li, X. Lu, X. Han, A. L. Rogach, C. Niu, *J. Mater. Chem. A* **2017**, *5*, 6817.
[42] Q. Ma, M. R. M. Rejab, J. P. Siregar, Z. Guan, *J. Compos. Mater.* **2021**, *55*, 2513.
[43] W. Zhang, C. Wu, C. Zhang, Z. Chen, *J. Bionic Eng.* **2012**, *9*, 330.
[44] K. Meng, X. Xiao, Z. Liu, S. Shen, T. Tat, Z. Wang, X. Lu, W. Ding, X. He, Jun Yang, J. Chen, *Adv. Mater.* **2022**, *34*, 2202478.
[45] H. Ouyang, J. Tian, G. Sun, Y. Zou, Z. Liu, H. Li, L. Zhao, B. Shi, Y. Fan, Y. Fan, Z. L. Wang, Z. Li, *Adv. Mater.* **2017**, *29*, 1703456.
[46] C. Yao, T. Sun, S. Huang, M. He, B. Liang, Z. Shen, X. Huang, Z. Liu, H. Wang, F. Liu, H. Chen, X. Xie, *ACS Nano* **2023**, *17*, 24242.
[47] H. D. Conway, *J. Appl. Mech.* **1961**, *28*, 288.
[48] K. Stephenson, *Not. Am. Math. Soc.* **2003**, *50*, 1376.
[49] Z. Zhang, T. Lu, D. Yang, S. Lu, R. Cai, W. Tan, *Nano Lett.* **2021**, *21*, 9030.
[50] Z. Zhang, S. Lu, R. Cai, W. Tan, **2021**, *38*, 101202.

